Coupled Thermal-Structural Analysis and Structural Optimization of the Diaphragm of a Diaphragm Compressor for a Hydrogen Refueling Station

Tao Li[1,2,3,*], Wei Hu[1], Haodong Luo[1], Mingxin Li[2,*], Yudong Hou[2] and Qingchao Sun[3]

[1] School of Mechanical Engineering, Zhengzhou University of Aeronautics, Zhengzhou, 450046, China

[2] Censtar H2-Electricity Science & Technology Zhengzhou Co., Ltd., Zhengzhou, 450000, China

[3] School of Mechanical Engineering, Dalian University of Technology, Dalian, 116024, China

INFORMATION

Keywords:
Hydrogen refueling station
diaphragm compressor
diaphragm
coupled thermal-structural analysis
structural optimization

DOI: 10.23967/j.rimni.2025.10.65051

SCIPEDIA
Revista Internacional de Métodos Numéricos para Cálculo y Diseño en Ingeniería
RIMNI

Coupled Thermal-Structural Analysis and Structural Optimization of the Diaphragm of a Diaphragm Compressor for a Hydrogen Refueling Station

Tao Li[1,2,3,*], Wei Hu[1], Haodong Luo[1], Mingxin Li[2,*], Yudong Hou[2] and Qingchao Sun[3]

[1]School of Mechanical Engineering, Zhengzhou University of Aeronautics, Zhengzhou, 450046, China

[2]Censtar H2-Electricity Science & Technology Zhengzhou Co., Ltd., Zhengzhou, 450000, China

[3]School of Mechanical Engineering, Dalian University of Technology, Dalian, 116024, China

ABSTRACT

Diaphragm fatigue fracture stands as one of the primary failure modes in hydrogen refueling station diaphragm compressors, urgently requiring systematic investigation into the mechanical properties and fatigue reliability of diaphragms under actual service conditions. However, due to the complex contact state between the diaphragm and the gas cavity cover plate (gas passage, gas hole)/oil cavity support plate and oil distribution plate (oil passage, oil hole), it is difficult to accurately obtain the stress distribution state of the diaphragm. In this study, we conducted material property experiments on the diaphragm to characterize its constitutive parameters. A refined numerical simulation model of the cover plate-diaphragm-support plate was established to analyze the mechanical properties of the diaphragm group under different conditions. The influence of diaphragm thickness on stress distribution and fatigue life was also explored. The results indicated that high stress distribution areas were mainly concentrated in the cavity transition zone and in the overlapping area of the diaphragm and gas passage/oil passage. The temperature inside the diaphragm compressor cavity had a significant impact on the stress level of the diaphragm. When the cavity temperature reached 300°C, the maximum von Mises stress reached 1286 MPa. The optimization results of diaphragm thickness indicated that when the diaphragm thickness was within the range of [0.3, 0.5 mm], the diaphragm was at a low stress service level; considering both the fatigue life and deflection performance of the diaphragm, the diaphragm thickness should be selected as thick as possible within the range of [0.3, 0.5 mm]. The numerical simulation model of the diaphragm compressor and the structural optimization design method of the diaphragm proposed in this article have significant engineering implications for improving the fatigue life of diaphragm compressor diaphragms.

OPEN ACCESS

Received: 02/03/2025

Accepted: 13/05/2025

Published: 14/07/2025

DOI
10.23967/j.rimni.2025.10.65051

Keywords:
Hydrogen refueling station
diaphragm compressor
diaphragm
coupled thermal-structural analysis
structural optimization

*Correspondence: Tao Li, Mingxin Li (litao@zua.edu.cn, limxzxr@163.com).

1 Introduction

As a core component of hydrogen refueling stations, diaphragm compressors account for more than 30% of the total cost [1,2]. The lifespan and efficiency of high-pressure diaphragm compressors directly determine the operating costs, performance, and safety of hydrogen refueling stations [3,4]. During the service process of diaphragm compressors, the diaphragm undergoes periodic deformation under the action of alternating cyclic loads, moving between the top dead center (closely adhering to the cavity surface of the cover plate) and the bottom dead center (closely adhering to the cavity surface of the support plate and the oil distribution plate) (Fig. 1a–c). This deformation is constrained by the cavity surface of the gas cavity cover plate and the cavity surface of the oil cavity support plate, resulting in high local stress at the gas hole, gas passage, oil hole, and oil passage, leading to fatigue failure of the diaphragm [5,6]. Numerous engineering examples of hydrogen refueling stations indicate that cracks and fractures in diaphragms (as shown in Fig. 1d–f) frequently lead to premature failure, seriously affecting the operational efficiency and equipment safety of hydrogen refueling stations [7]. Therefore, there is an urgent need to explore the mechanical characteristics of diaphragm compressors' diaphragms under real service conditions and develop structural optimization design methods to enhance the fatigue life of diaphragms, reduce the probability of diaphragm failure, and ultimately improve the efficiency and service life of diaphragm compressors.

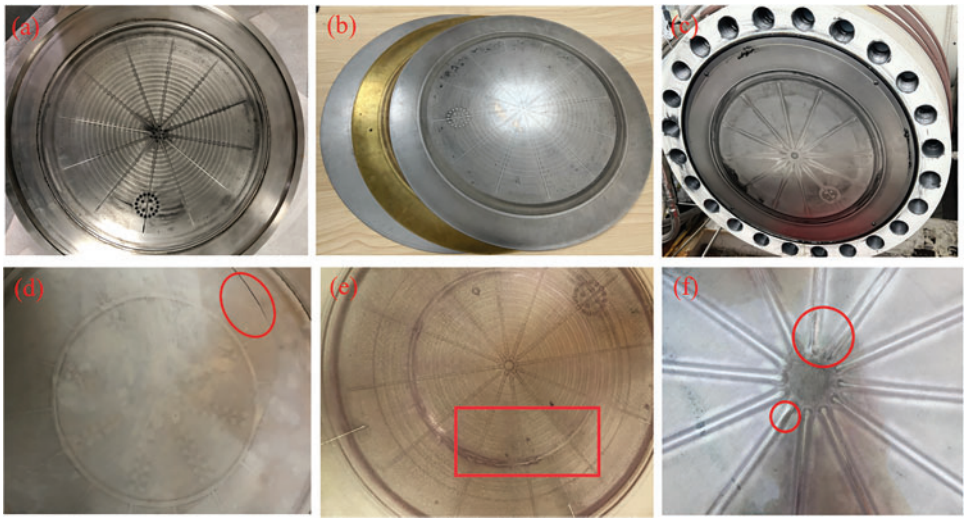

Figure 1: Typical failure forms of diaphragm compressors diaphragm: (a) gas cavity cover plate; (b) diaphragm group; (c) oil cavity support plate; (d) diaphragm splits; (e) copper sheet crack; (f) diaphragm crack and crumbling pointing

Currently, scholars both domestically and internationally have primarily conducted research on the mechanical properties of diaphragms, volumetric efficiency, optimization of diaphragm cavity structure, and fault diagnosis of diaphragm compressors, utilizing theoretical and experimental methods. Jia et al. proposed a theoretical analysis method for diaphragm stress that combines the theory of large deflection of thin plates with the theory of small deflection of thin plates, subsequently studying the motion patterns of the diaphragm during service [8,9]. Lee et al. improved the durability of hydrogen compressor diaphragms by applying a Teflon coating to stainless steel 301, and verified through finite element analysis that it outperforms Inconel 718 in terms of hardness, strength, and frictional resistance [10]. Li et al. simulated and analyzed the von Mises stress and axial deformation

patterns of the diaphragm under varying oil-gas pressure differences [11]. Ren et al. investigated the compressibility of hydraulic oil and the impact mechanism of temperature on the volumetric efficiency of diaphragm compressors through a combination of theoretical analysis and experiments, proposing corresponding optimization strategies [12,13]. Some scholars have optimized the gas cavity profile of diaphragm compressors to enhance their operational efficiency and maximum output pressure [14,15]. Significant achievements have been made in the fault diagnosis of diaphragm compressors, such as non-destructive diagnosis methods based on acoustic emission [16,17], and detection methods for diaphragm motion status based on hydraulic oil pressure [18]. Additionally, scholars have proposed methods based on characteristic event signals to identify typical abnormal conditions such as excessive oil pressure, slight oil pressure deficiency, and severe oil pressure deficiency, thereby improving the compressor's operational efficiency [19,20].

Due to the presence of numerous wear parts in diaphragm compressors, such as oil/gas valve seals, piston rings, and diaphragms [21], failures often occur due to fatigue, including issues with pipelines or valves [22], decreased oil pressure [23], and diaphragm rupture [24]. Users are particularly concerned about diaphragm rupture, as it not only endangers the safety of the entire system but also leads to extensive maintenance work and requires a long time for repair. Over the past few decades, researchers have made numerous efforts to enhance the fatigue life of diaphragms. Wang et al. found that during compressor operation, the exhaust port experiences the highest temperature, which not only induces plastic deformation but also causes significant stress concentration. The high-temperature stress can reach the material's strength limit [25]. To improve the lifespan of the diaphragm, some scholars have investigated the impact of the contours of the gas and oil cavities on the diaphragm's lifespan and designed new cavity types to enhance the diaphragm's contact state and stress distribution. However, the improvements remain limited, with the principal stress of diaphragms reduced by only approximately 10% [26].

However, in the current actual service process, the rupture of the diaphragm has become the main failure of the diaphragm compressor. The main reason is the premature fatigue fracture caused by excessive additional stress generated at the contact points between the diaphragm and the baffle plate, such as gas holes and oil passages [27]. Wear of the piston ring, stalling of the oil pressure limiter, and drastic changes in ambient temperature can all lead to high additional stress caused by the collision between the diaphragm and the baffle plate. At the same time, due to the particularity of the hydrogen medium, strict sealing requirements are imposed on the oil cavity and gas cavity, making it difficult to accurately monitor the pressure inside the cavity and the movement pattern of the diaphragm using built-in sensors. Therefore, it is urgent to establish an accurate contact mechanics model of the diaphragm compressor diaphragm to explore the motion state and stress distribution of the diaphragm.

To address the high failure rate of diaphragm rupture in diaphragm compressors, this study establishes a high-fidelity numerical simulation model of the gas cavity-diaphragm-oil cavity system based on actual service conditions, fully considering the influence of additional stresses caused by grooves and holes in the gas/oil cavities. Utilizing the sequential coupling method, computational complexity in the individual physical analyses is kept to minimal and thermal and structural analysis are coupled through unidirectional data transfer, enabling stepwise solution of the two physical fields [28] to investigate the mechanical properties and stress distribution patterns of the diaphragm. Furthermore, by analyzing stress levels and fatigue life of diaphragms with varying thicknesses, an optimized diaphragm structural design method [29] is proposed, balancing compressor efficiency and fatigue life. This approach holds significant engineering implications for enhancing diaphragm service life and reducing maintenance costs in hydrogen refueling stations.

2 Models and Methods

2.1 Diaphragm Structure and Load

The diaphragm compressor is primarily composed of the gas cavity cover plate, oil cavity support plate, oil distribution plate, diaphragm, and other components, exhibiting an upper-lower structure. The flange connects the upper and lower parts through bolts, with the intermediate structure being the diaphragm, typically consisting of three thin layers: the upper and lower layers are made of stainless steel, and the middle layer is made of copper. The diaphragm is positioned in the middle, dividing the diaphragm cavity into a gas cavity and an oil cavity, as shown in Fig. 2. During the intake phase, the diaphragm moves to the bottom dead center and comes into contact with the oil distribution plate; during the exhaust phase, the diaphragm moves to the top dead center under the action of hydraulic oil. Stress concentration and high additional stress are generated during the contact process of the diaphragm with the gas cavity and oil distribution plate, which in turn leads to fatigue damage and failure of the diaphragm.

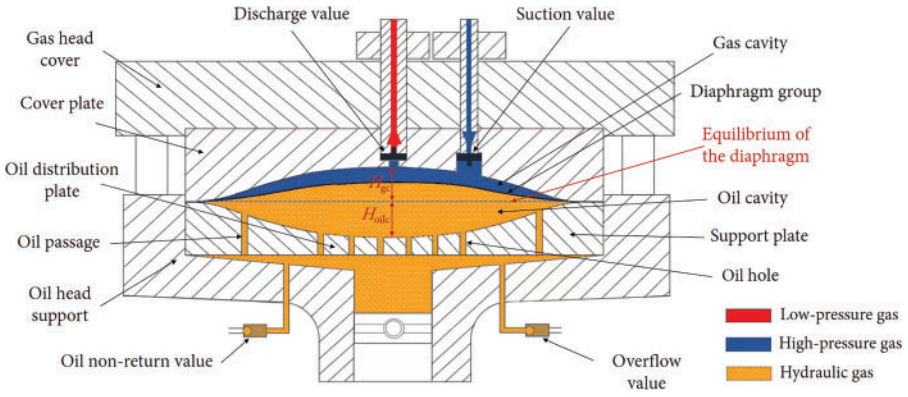

Figure 2: Structure of diaphragm compressors

The working load borne by the diaphragm primarily arises from the pressure difference between the gas and oil sides. During the exhaust phase, given that the exhaust pressure ranges from approximately 20 to 45 MPa, the maximum oil pressure when the diaphragm moves to the top dead center can reach 55 MPa, with a maximum oil-gas pressure difference of up to 35 MPa. In the intake phase, the minimum oil pressure after the diaphragm reaches the bottom dead center remains unaffected by the suction pressure. Therefore, when the maximum suction pressure is 20 MPa, the minimum oil pressure during this phase is 4.5 MPa, and the gas-oil pressure difference is 15.5 MPa.

2.2 Experimental Methods

To accurately obtain the mechanical performance parameters of the diaphragm, a static mechanical performance experiment was conducted on the diaphragm of the diaphragm compressor. The experimental setup is illustrated in Fig. 3. The test results provide the mechanical property parameters of the diaphragm, as summarized in Table 1.

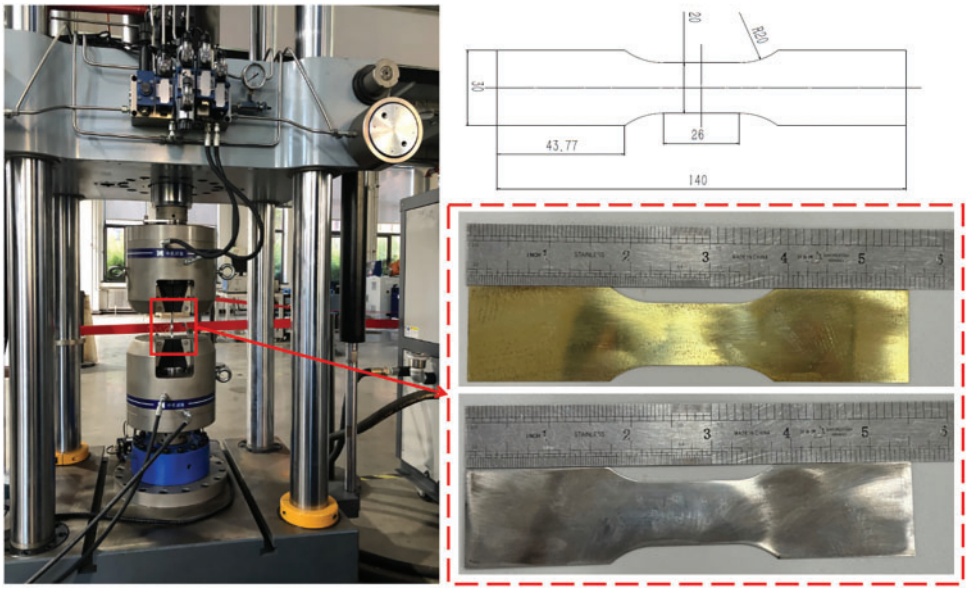

Figure 3: Mechanical property test of diaphragm

Table 1: Mechanical performance parameters of compressor diaphragms

	Gas/Oil side diaphragm	Gas/Oil side diaphragm
Material	Inconel718 (GH4169)	Brass
Density (kg/m^3)	8190	8267
Young's modulus (MPa)	200,000	99,950
Poisson's ratio	0.300	0.345
Tensile strength (MPa)	1518	372
Yield strength (MPa)	1315	367

2.3 Numerical Simulation Model

To investigate the motion patterns and mechanical characteristics of the diaphragm in a diaphragm compressor under service conditions, a refined contact numerical simulation model of the diaphragm compressor's gas cavity cover plate—diaphragm group—oil cavity support plate and oil distribution plate was established based on the finite element software Abaqus, as shown in Fig. 4. The material performance parameters of key components of the diaphragm compressor were set according to Table 1.

Structural analysis of the diaphragm is conducted using a General Static step, while the coupled thermal-structural analysis employs a Temperature-Displacement Coupled step for sequential coupling analysis. The cover plates, support plates, oil distribution plate, and the edges of the diaphragm were set as fully fixed constraints. The upper and lower surfaces of the diaphragm within the chamber were subjected to gas pressure and oil pressure, respectively. Surface-to-surface contact was defined between the diaphragm and components including the cover plates, support plates, and oil distribution plate.

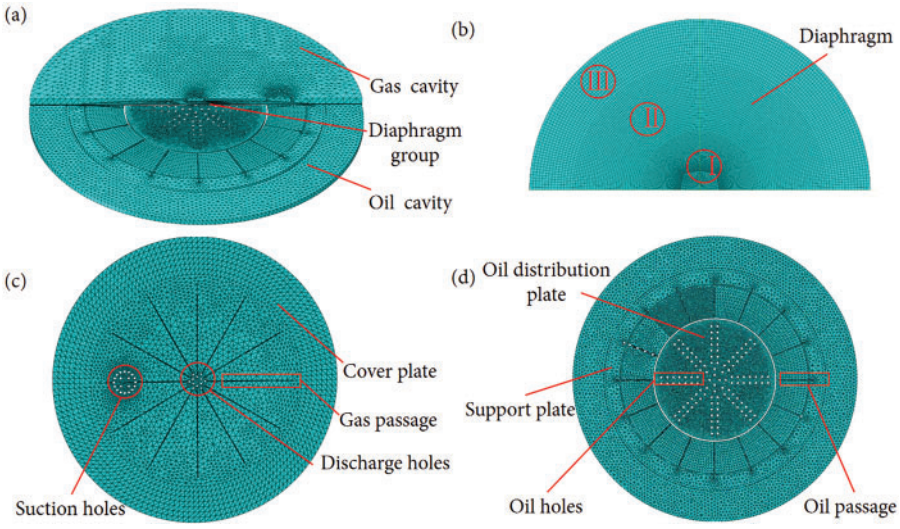

Figure 4: Numerical simulation model of gas cavity-diaphragm-oil cavity for the diaphragm compressor (a–d)

To verify the mesh independence of the finite element analysis results, an initial mesh containing 394,322 elements was used. When the mesh density was reduced to 355,406 elements, the stress field variation rate reached 5.1%, indicating poor convergence. Subsequent refinement of the mesh to 432,509 and 453,345 elements revealed stress field variation rates below 1%, demonstrating sufficient convergence. Based on these findings, the mesh configuration with 432,509 elements (corresponding to 667,939 nodes) was selected as the optimal choice for subsequent analyses. In the numerical simulation model, the cover plate, support plate, and oil distribution plate are meshed with unstructured tetrahedral elements (10-node quadratic tetrahedrons), while the diaphragm employs structured hexahedral elements (8-node reduced integration hexahedrons). Through Analysis Checks (including mesh integrity issues, element type compatibility, model completeness, boundary condition validity, and contact pair settings), the mesh quality was validated, showing a 0% error/warning rate for the three-layer diaphragms and a 0% error rate with a warning rate below 3% for components including cover plates, support plates, and oil distribution plates, indicating satisfactory compliance with computational requirements. The contact type between the cover plate, support plate, oil distribution plate, and diaphragm is surface-to-surface contact.

The load time history of the diaphragm compressor is shown in Fig. 5. The extreme service load conditions when the diaphragm moves to the upper and lower dead centers are analyzed, and the two working conditions are listed in Table 2. The numerical simulation model of the diaphragm compressor cavity-diaphragm contact is illustrated.

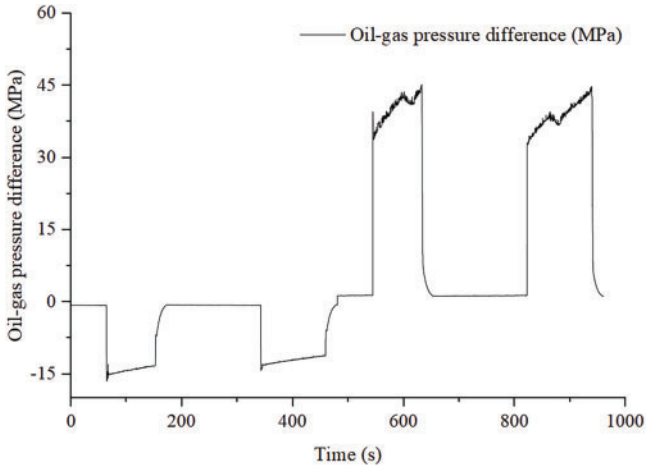

Figure 5: Diaphragm compressor load time history diagram

Table 2: Extreme load condition of diaphragm compressor

Condition	1 (Suction phase)	2 (Discharge phase)
Pressure difference (MPa)	−15.5	35.0

2.4 Finite Element Discretization and Sequential Coupling Method

This section presents the finite element discrete form of the governing equations for heat transfer and structural mechanics and describes the steps to implement the sequential coupling method.

2.4.1 Discretization of the Thermal Model

The transient heat transfer equation is:

$$\rho c_p \frac{\partial T}{\partial t} = \nabla \cdot (k \nabla T) + Q \tag{1}$$

where ρ is the material density, c_p is the specific heat capacity, k is the thermal conductivity, T is the temperature field, and Q is the internal heat source term. Temperature field approximation using shape functions:

$$T(x,t) \approx \sum_{i=1}^{n} N_i(x)\, T_i(t) = \mathbf{N}^T \mathbf{T}(t) \tag{2}$$

where $N_i(x)$ is the shape function, $T_i(t)$ is the node temperature, $\mathbf{N}$ is the shape function vector, and $\mathbf{T}$ is the node temperature vector. The Galerkin method is applied to obtain the matrix equation:

$$\mathbf{C}_T \frac{d\mathbf{T}}{dt} + \mathbf{K}_T \mathbf{T} = \mathbf{F}_T \tag{3}$$

wherein $\mathbf{C}_T$, $\mathbf{K}_T$ and $\mathbf{F}_T$ are heat capacity matrix, heat conduction matrix and heat load vector, respectively. The specific form of matrix is as follows:

$$\mathbf{C}_T = \int_\Omega \rho c_p \mathbf{N}\mathbf{N}^T d\Omega \tag{4}$$

$$\mathbf{K}_T = \int_\Omega k\nabla\mathbf{N}\left(\nabla\mathbf{N}\right)^T d\Omega \tag{5}$$

$$\mathbf{F}_T = \int_\Omega \mathbf{N}Q d\Omega + \int_{\Gamma_N} \mathbf{N}q d\Gamma \tag{6}$$

where Γ_N is the Neumann boundary and q is the boundary heat flux. The implicit Euler method is used to discretize the transient term:

$$\left(\frac{\mathbf{C}_T}{\Delta t} + \mathbf{K}_T\right)\mathbf{T}^{n+1} = \frac{\mathbf{C}_T}{\Delta t}\mathbf{T}^n + \mathbf{F}_T^{n+1} \tag{7}$$

where Δt is the time step size, and $\mathbf{T}^n$, $\mathbf{T}^{n+1}$ are the temperature vectors at the n-th and $(n+1)$-th time steps.

2.4.2 Discretization of the Structural Model

The static balance equation and thermal stress constitutive relation are as follows:

$$\nabla\cdot\boldsymbol{\sigma} + \mathbf{f} = 0, \boldsymbol{\sigma} = \mathbf{C}\left(\boldsymbol{\varepsilon} - \alpha\Delta T\mathbf{I}\right) \tag{8}$$

where $\boldsymbol{\sigma}$ is Cauchy stress tensor, $\mathbf{f}$ is volume force, $\mathbf{C}$ is elastic stiffness matrix, $\boldsymbol{\varepsilon}$ is total strain tensor, α is coefficient of thermal expansion and ΔT is temperature variation. The displacement field is discretized in space, approximately as follows:

$$\mathbf{u}\left(x\right) \approx \sum_{i=1}^{n} N_i\left(x\right)\mathbf{u}_i = \mathbf{N}^T\mathbf{u} \tag{9}$$

where $\mathbf{u}_i$ is the displacement vector of node. The strain-displacement relation is:

$$\boldsymbol{\varepsilon} = \mathbf{B}\mathbf{u}, \mathbf{B} = \nabla\mathbf{N} \tag{10}$$

where $\mathbf{B}$ is the strain-displacement matrix. The discrete balance equation is:

$$\mathbf{K}_s\mathbf{u} = \mathbf{F}_S^{mesh} + \mathbf{F}_S^{thermal} \tag{11}$$

where $\mathbf{K}_s$, $\mathbf{F}_S^{mesh}$ and $\mathbf{F}_S^{thermal}$ are structural stiffness matrix, mechanical load vector and thermal load vector, respectively, which are specifically expressed as follows:

$$\mathbf{K}_S = \int_\Omega \mathbf{B}^T\mathbf{C}\mathbf{B} d\Omega \tag{12}$$

$$\mathbf{F}_S^{thermal} = \int_\Omega \mathbf{B}^T\mathbf{C}\alpha\Delta T\mathbf{I}\, d\Omega \tag{13}$$

$$\mathbf{F}_S^{mesh} = \int_\Omega \mathbf{N}^T\mathbf{f} d\Omega + \int_{\Gamma_t} \mathbf{N}^T\mathbf{t} d\Gamma \tag{14}$$

where Γ_t is the boundary of applied surface force and $\mathbf{t}$ is the surface traction force.

2.4.3 Sequential Coupling Method

Sequential coupling is divided into two steps to realize the thermal-structure interaction. First, the thermal analysis is performed to solve the discrete Eq. (7) to obtain the transient temperature field **T**. Then, the structural analysis is performed to calculate the thermal strain from the temperature field:

$$\boldsymbol{\varepsilon}_{thermal} = \alpha \left(\mathbf{T} - T_{ref}\right) \mathbf{I} \tag{15}$$

where T_{ref} is the initial temperature without thermal strain. Finally, the thermal strain is input into the structural model as the initial strain, and the displacement field **u** is obtained by solving Eq. (11).

3 Result

3.1 Structural Analysis

Based on the numerical simulation model of the diaphragm compressor's gas cavity-diaphragm-oil cavity contact (with three diaphragms each having a thickness of 0.4 mm), structural mechanics analysis was conducted to obtain the von Mises stress and the first principal stress of the diaphragm on the gas side/oil side of the diaphragm compressor under different operating conditions, as shown in Figs. 6 and 7.

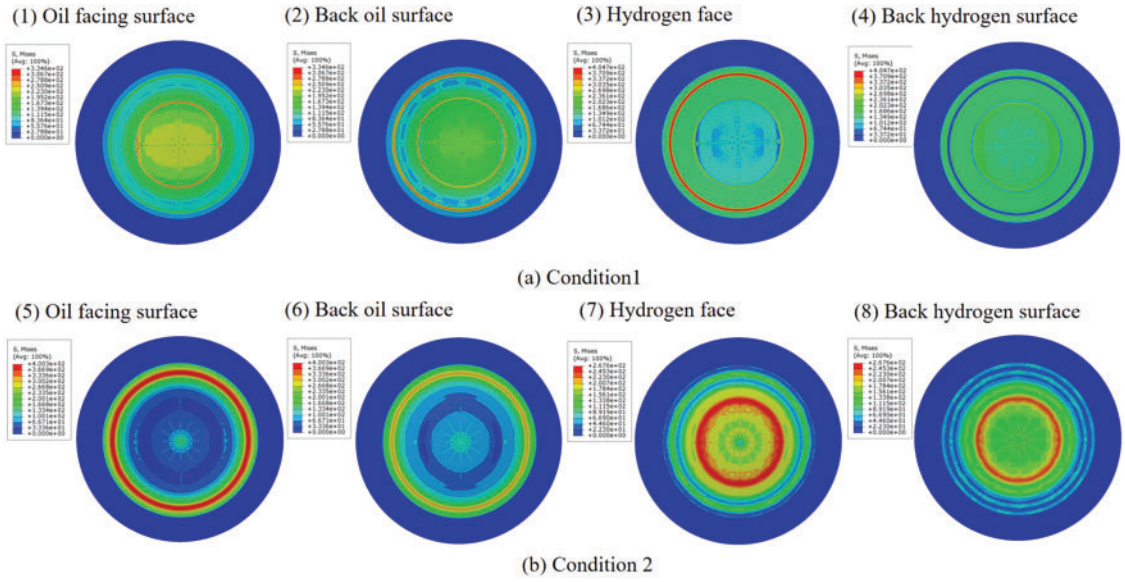

Figure 6: Von Mises stress (MPa) distribution of diaphragms under different working conditions (a,b)

As can be seen from Figs. 6 and 7, under condition 1 (gas-oil pressure difference of 15.5 MPa, with the diaphragm group attached to the oil cavity): the maximum von Mises stress of the oil-side diaphragm is 334.6 MPa, and the first principal stress is 345.9 MPa. The maximum von Mises stress of the hydrogen-side diaphragm is 404.7 MPa, and the first principal stress is 432.7 MPa. Under condition 2 (oil-gas pressure difference of 35 MPa, with the diaphragm group attached to the inlet cavity): the maximum von Mises stress of the oil-side diaphragm is 400.3 MPa, and the first principal stress is 392.4 MPa. The maximum von Mises stress of the hydrogen-side diaphragm is 267.6 MPa, and the first principal stress is 255.1 MPa. Under both conditions, the first principal stress of the diaphragms on both the gas and oil sides is in the radial direction.

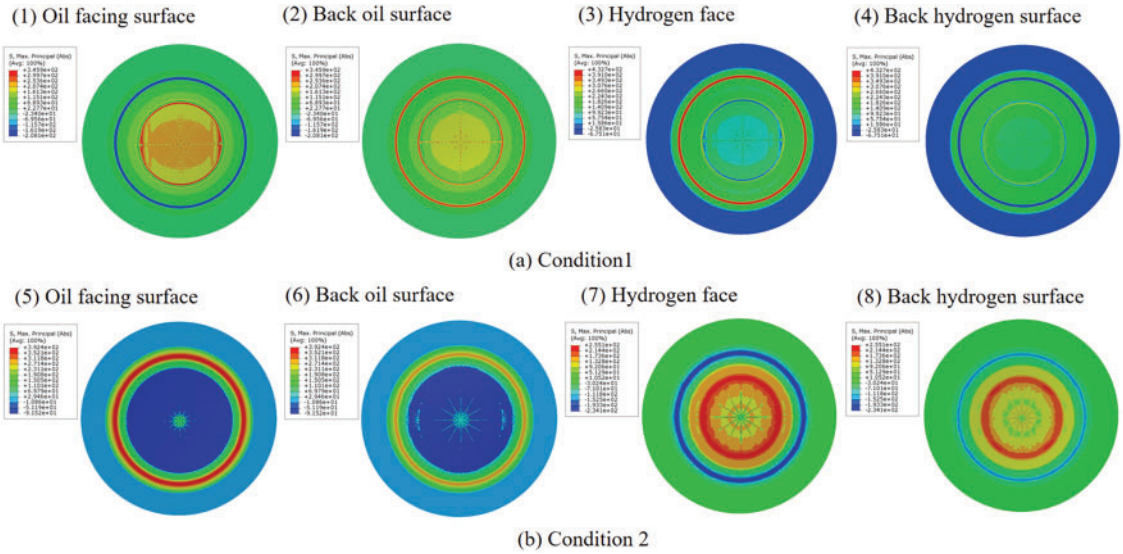

Figure 7: First principal stress (MPa) distribution of diaphragms under different working conditions (a,b)

3.2 Thermal-Structure Analysis

During operation, the diaphragm compressor in the hydrogen refueling station repeatedly pressurizes hydrogen, generating a large amount of heat. Under the coupled thermal-structural effect, the diaphragm moves up and down reciprocally. To accurately obtain the mechanical characteristics of the diaphragm compressor's diaphragm under extreme service conditions, a numerical model for coupled thermal-structural analysis of the diaphragm was established. The mechanical characteristics of the diaphragm under different temperature fields were explored.

The temperature-displacement coupled analysis step was utilized. Surface convection conditions with a film coefficient of 0.1 mW/(mm^2·K) were applied to all internal cavity surfaces to define the thermal boundary conditions. Additionally, radiation boundary conditions of the "To Ambient" type with an emissivity of 0.6 were imposed on all external surfaces of the numerical model. The related thermal parameters of the diaphragm are shown in Table 3. The stress contour plot of the diaphragm is shown in Fig. 8, and the maximum von Mises stress under different conditions is shown in Table 4.

Table 3: Diaphragm thermal parameters [30]

Parameters	100°C	200°C	300°C
Young's modulus (MPa)	196,500	193,000	181,000
Poisson's ratio	0.300	0.303	0.307
Expansion coefficient (K^{-1})	1.89E−05	1.91E−05	1.93E−05
Specific heat (mJ/(t·K))	4.52E8	4.73E8	4.89E8
Thermal conductivity (mW/(mm·K))	14.5	16.0	17.2

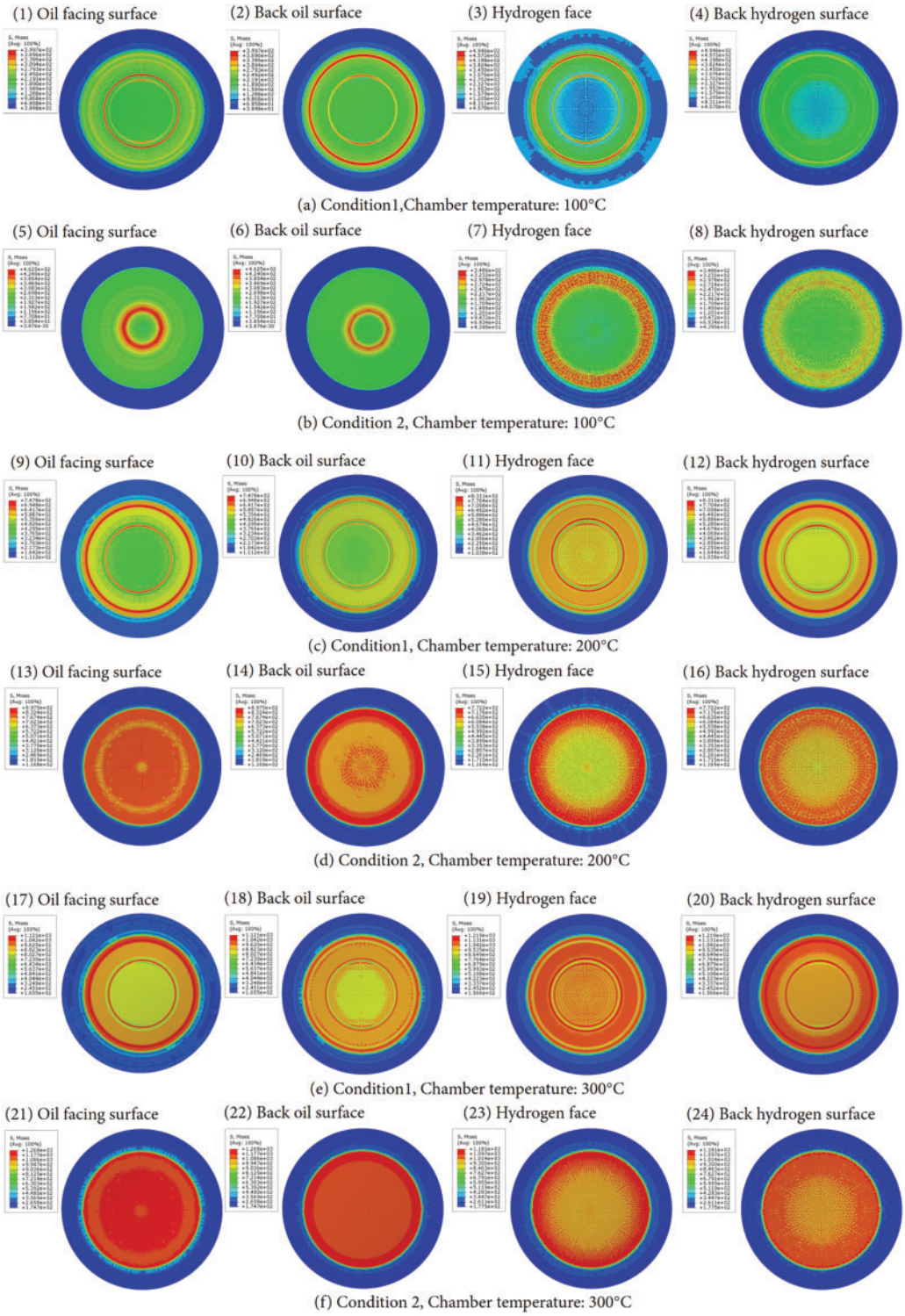

Figure 8: Von Mises stress (MPa) distribution of diaphragms under various coupled thermal-structural conditions (a–f)

Table 4: Von Mises stress (SEQV) of diaphragm under two working conditions under thermal-mechanical coupling

Cavity temperature (°C)	Oil side diaphragm SEQV (MPa)		Gas side diaphragm SEQV (MPa)	
	Condition 1	Condition 2	Condition 1	Condition 2
20 (Normal temperature)	334.6	**400.3**	404.7	267.6
100	399.7	**462.5**	494.6	348.6
200	747.8	**897.5**	831.1	772.2
300	1121.0	**1268.0**	1219.0	1181.0

3.3 Contact Analysis

As shown in Sections 3.2 and 3.3, the maximum stress in the diaphragm is typically concentrated at the groove areas due to additional stresses induced by contact interactions. To further investigate the mechanisms affecting the diaphragm's lifespan, its contact pressure distribution and sliding behavior (which governs wear evolution) were analyzed based on observed stress distribution patterns. Since the spatial distributions of contact pressure and sliding wear under various operating conditions are similar, the coupled thermal-structural conditions at 100°C was selected as a representative case. The corresponding contact pressure distribution, tangential slip distribution, and contact status diagrams are illustrated in Figs. 9–11, respectively.

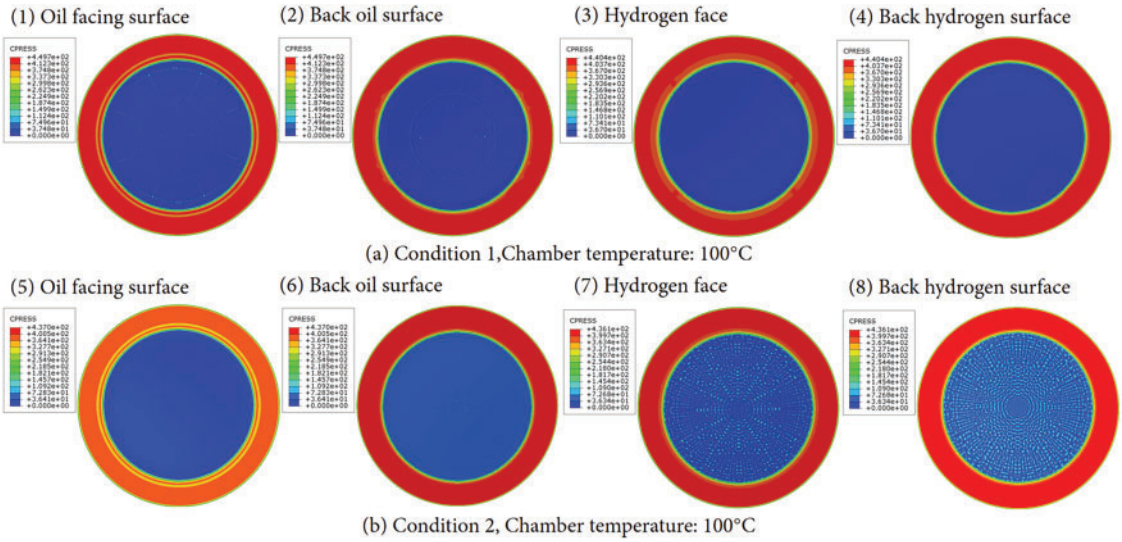

Figure 9: Contact pressure (N) distribution of the diaphragms under coupled thermal-structural conditions at 100°C (a,b)

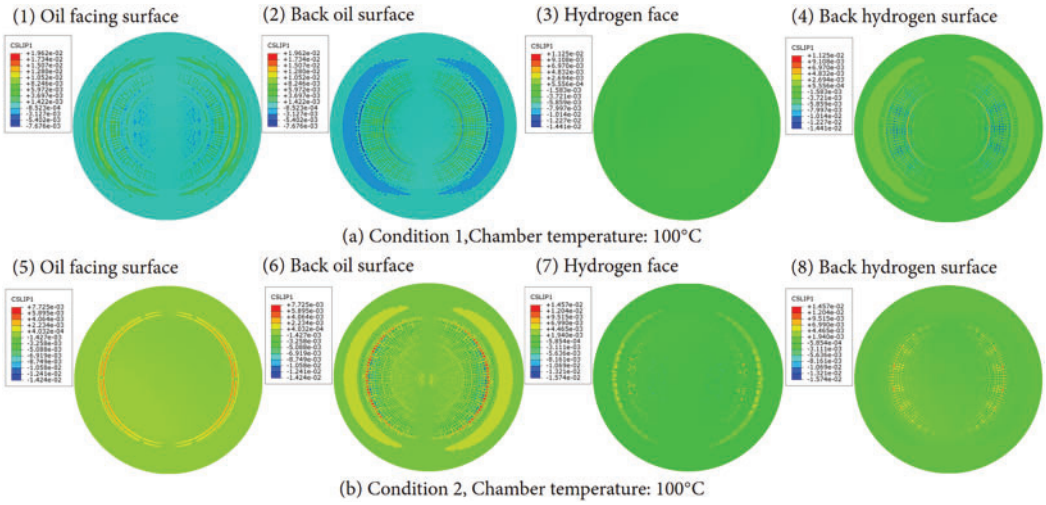

Figure 10: Tangential slip (mm) of diaphragms contact surface under coupled thermal-structural conditions at 100°C (a,b)

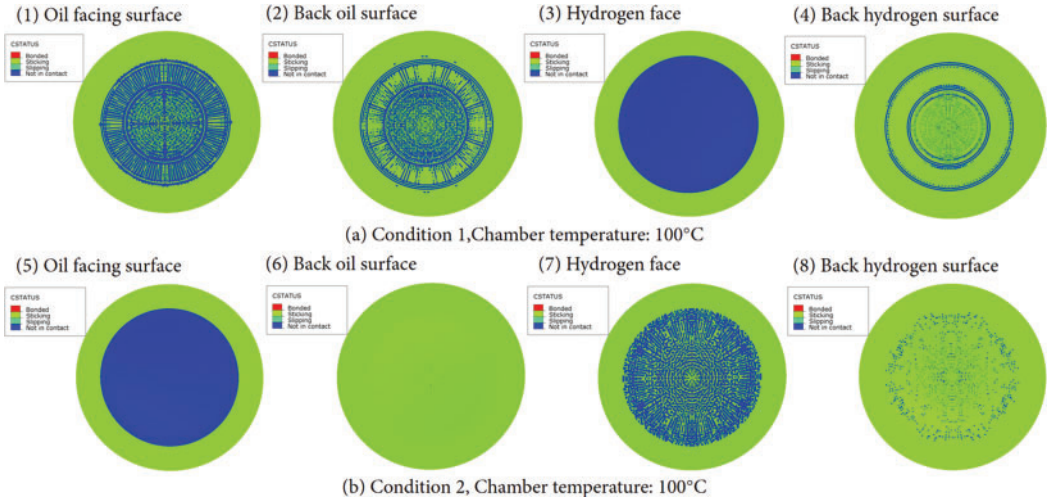

Figure 11: Diaphragms contact state diagram under coupled thermal-structural conditions at 100°C (a,b)

3.4 Structural Parameter Optimization

The diaphragm group consists of three layers of diaphragms made of different materials, with the upper and lower layers being made of stainless steel and the middle layer being made of copper. Under the same oil-gas pressure difference, as the thickness of the diaphragm decreases, the deflection of the diaphragm also decreases, reducing the bonding points and friction points caused by interlayer impact in the central area. Consequently, thinning the diaphragm helps lower its stress levels and enhances its fatigue life. However, excessively thin diaphragms exhibit low elasticity, are prone to fracture, and pose significant manufacturing challenges, while overly thick diaphragms suffer from poor flexural deformation performance. Therefore, by comprehensively considering the operating conditions of the compressor, optimizing the diaphragm thickness can effectively enhance its service life.

Establish numerical models of gas cavity-diaphragm group-oil cavity with different diaphragm thicknesses (the structural dimensions of the diaphragm group are shown in Table 5), then divide the diaphragm groups with different thicknesses into the same number and type of grids, and set the same material properties, loads, constraints, and boundary conditions. Conduct finite element analysis to obtain the stress variation patterns of the diaphragm groups under two extreme operating conditions (Condition 1, Condition 2), as shown in Fig. 12.

Table 5: Structural dimensions of diaphragm group (mm)

Sample	Gas side diaphragm	Intermediate diaphragm	Oil side diaphragm
1	0.30	0.30	0.30
2	0.30	0.40	0.30
3	0.35	0.35	0.35
4	0.35	0.40	0.35
5	0.40	0.40	0.40
6	0.45	0.40	0.45
7	0.45	0.45	0.45
8	0.50	0.40	0.50
9	0.50	0.50	0.50
10	0.60	0.60	0.60
11	0.80	0.80	0.80
12	0.90	0.90	0.90
13	1.00	1.00	1.00
14	1.05	1.05	1.05
15	1.10	1.10	1.10
16	1.15	1.15	1.15
17	1.20	1.20	1.20

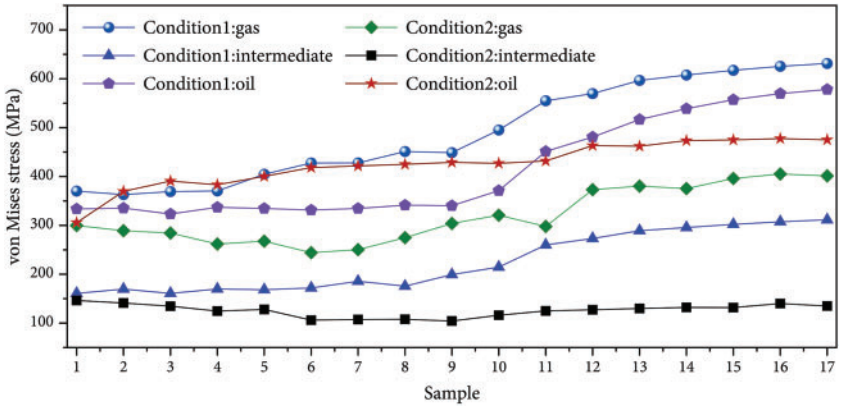

Figure 12: Von Mises stress variation diagram of different diaphragm structure

To further investigate the influence of diaphragm thickness on fatigue life, fatigue life simulation was performed on the diaphragm using fe-safe software based on the analytical results presented in Fig. 12. Taking Samples 1, 9, and 10 as examples (with three-layer diaphragm thicknesses of 0.30, 0.50, and 0.60 mm, respectively), the fatigue life of gas-side diaphragms under Condition 1 was calculated (as shown in Fig. 12, the gas-side diaphragm exhibits the maximum stress under Condition 1).

The finite element calculation result files from Abaqus were imported into fe-safe. Material properties were defined as Inconel 718 for the diaphragm with a correction factor of 1. Select the von Mises stress-based Goodman correction algorithm applicable to high-cycle fatigue, along with the load history illustrated in Fig. 5. The resulting fatigue life contour plots are presented in Fig. 13. The fatigue life values are presented in Table 6.

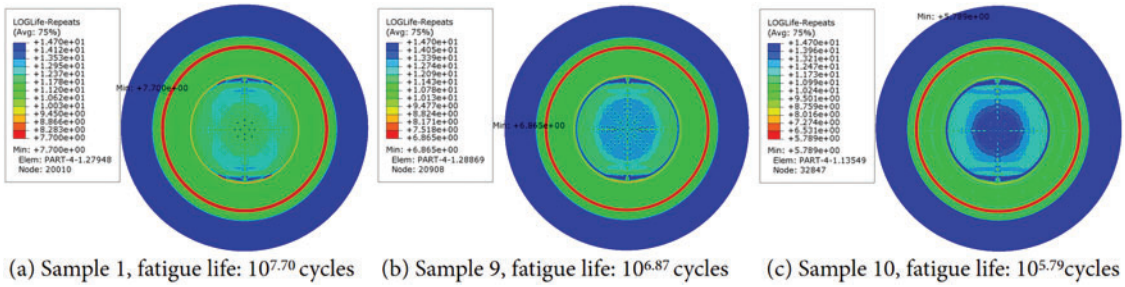

(a) Sample 1, fatigue life: $10^{7.70}$ cycles (b) Sample 9, fatigue life: $10^{6.87}$ cycles (c) Sample 10, fatigue life: $10^{5.79}$cycles

Figure 13: Fatigue life contour (a–c)

Table 6: Fatigue life (cycles) of samples 1, 9, and 10

Sample	Fatigue life (Cycles)
1 (The membrane thickness is 0.3 mm)	$10^{7.70}$
9 (The membrane thickness is 0.5 mm)	$10^{6.87}$
10 (The membrane thickness is 0.6 mm)	$10^{5.79}$

4 Discusses

Under two extreme service conditions (when the diaphragm moves to the top and bottom dead centers), the diaphragm group exhibits varying degrees of high stress concentration. On the gas side, this is mainly manifested in the transition area of the gas cavity and the distribution area of the gas passage, while on the oil side, it is mainly concentrated at the oil distribution groove of the oil distribution plate. When the diaphragm of the diaphragm compressor moves to the top and bottom dead centers, the maximum von Mises stress of the diaphragm is 400.3 and 404.7 MPa, respectively, and the maximum first principal stress is 392.4 and 432.7 MPa, respectively. The values of von Mises stress and maximum principal stress under the two extreme conditions are close, which meets the design requirements for equal lifespan of the gas-side diaphragm and oil-side diaphragm. The direction of the first principal stress is along the radial direction, which leads to the formation of circular or elliptical cracks from crack initiation to cracking in the diaphragm. The stress concentration of the diaphragm is located at the transition edge of the cavity, which is consistent with the frequent cracking locations observed in the current service process of the diaphragm (Fig. 1d), greatly reducing the service life of the diaphragm and the operational stability of the diaphragm compressor. In addition, Condition 1

and Condition 2 are used as key load points for designing the load spectrum when checking the fatigue strength or predicting the fatigue life of the compressor diaphragm.

The thermal-mechanical coupling analysis results of the diaphragm compressor diaphragm indicate that the temperature inside the diaphragm compressor cavity has a significant impact on the stress distribution of the diaphragm. As the cavity temperature increases, the stress level of the diaphragm increases nonlinearly. Taking the oil-side diaphragm under condition 2 as an example, when the cavity temperature stabilizes at 100°C, the stress of the gas-side diaphragm increases by 15.5% compared to the normal temperature state (20°C). When the cavity temperature increases to 200°C and 300°C, the stress of the diaphragm increases by 124.2% and 216.8% respectively compared to the normal temperature state. When the cavity temperature reaches 300°C, the maximum von Mises stress of the diaphragm reaches 1286 MPa, which is close to the yield strength of the diaphragm, easily cause diaphragm fracture and compromise the normal operation of the diaphragm compressor. Therefore, in the design process of the diaphragm head of ultra-high pressure diaphragm compressors, it is necessary to optimize the hydrogen cooling channel and high temperature warning system to prevent the diaphragm cavity temperature from being too high, which can cause high stress operation of the diaphragm and further lead to premature fatigue damage of the diaphragm.

As demonstrated in Figs. 9–11, the maximum contact pressure on the diaphragm is concentrated at its edge clamping surface; sliding predominantly occurs in regions of elevated stress where the diaphragm contacts the cavity wall; and extensive areas of the contact surface remain detached from the cavity wall, resulting in suboptimal contact conditions. Simulation results demonstrate that the numerical predictions of diaphragm contact and wear states align with experimental observations, providing critical insights into the wear failure mechanisms of diaphragms.

The optimization analysis of the diaphragm thickness for the diaphragm compressor (Fig. 12) indicates that the diaphragm thickness has a significant impact on the stress state of both the oil-side diaphragm and the gas-side diaphragm, exhibiting strong nonlinearity. The thickness of the intermediate copper sheet has a relatively weak impact on its stress, which remains basically stable. The analysis results from 17 sample groups show that as the diaphragm thickness increases, the von Mises stress of both the oil-side diaphragm and the gas-side diaphragm continuously increases. When the diaphragm thickness exceeds 0.5 mm, the diaphragm stress increases sharply. When the diaphragm thickness reaches 1 mm, the diaphragm stress remains basically unchanged, forming a stable range. When the diaphragm thickness is within the range of [0.3, 0.5 mm], the diaphragm stress maintains a slow increasing trend as the diaphragm thickness increases, with the maximum increase in stress for the upper and lower diaphragms being less than 20%. Diaphragm failure in diaphragm compressors is a typical high-cycle fatigue failure mode, requiring a cyclic fatigue life generally exceeding 10^7 cycles. According to the stress variation patterns across diaphragm thicknesses and the fatigue life analysis results of Samples 1, 9, and 10 (Fig. 13), the diaphragm thickness must be less than 0.5 mm to meet fatigue life requirements. However, excessively thin diaphragms exhibit reduced elasticity (prone to fracture) and are more susceptible to corrosion, oxidation, or temperature effects during actual operation, accelerating fatigue crack propagation, while excessively thick diaphragms demonstrate poor deflection performance and a sharp stress increase. Therefore, considering both the fatigue life and flexural performance of the diaphragm, a thicker diaphragm should be selected in the low stress distribution range ([0.3, 0.5 mm]) for diaphragm thickness design.

5 Conclusions

The primary research conducted in this study involves developing a high-fidelity numerical simulation model under extreme operating conditions of the diaphragm, based on the service requirements of ultra-high-pressure diaphragm compressors in hydrogen refueling stations and integrated with mechanical property testing of the diaphragm. This model investigates stress distribution patterns, sliding behavior under coupled thermal-structural, and the influence of diaphragm thickness on stress states, providing critical guidance and boundary conditions for the structural design and fatigue life prediction of diaphragms and their cavities in hydrogen refueling stations. The important conclusions are as follows:

(1) Under the normal temperature limit operating condition, the maximum von Mises stress and the first principal stress of the diaphragm of the compressor are 404.7 and 432.7 MPa, respectively, with the direction of the first principal stress being along the radial direction. The high stress of the diaphragm on the gas side and oil side is mainly distributed in the transition area between the diaphragm cavity flange and the gas cavity, which is basically consistent with the location of most ruptures during actual service. Therefore, in the design process of the diaphragm cavity, it is necessary to optimize the transition radius of the starting arc of the diaphragm cavity profile to reduce stress concentration.

(2) The temperature inside the diaphragm compressor's membrane cavity has a significant impact on the stress distribution of the diaphragm. As the temperature of the membrane cavity increases, the stress level of the diaphragm increases nonlinearly. When the cavity temperature reaches 300°C, the maximum von Mises stress of the diaphragm reaches 1286 MPa, which is close to the yield strength of the diaphragm, easily cause diaphragm fracture and compromise the normal operation of the diaphragm compressor. Therefore, it is imperative to optimize the hydrogen cooling channels and implement a high-temperature early warning system to prevent excessive temperature in the diaphragm cavity, which would result in high-stress operation of the diaphragm and lead to premature fatigue damage.

(3) The maximum contact pressure on the diaphragm is concentrated at its edge clamping surface; sliding predominantly occurs in regions of elevated stress where the diaphragm contacts the cavity wall; and extensive areas of the contact surface remain detached from the cavity wall, resulting in suboptimal contact conditions. Simulation results demonstrate that the numerical predictions of diaphragm contact and wear states align with experimental observations, providing critical insights into the wear failure mechanisms of diaphragms.

(4) The thickness of the diaphragm significantly affects the stress state and fatigue life of both the oil-side diaphragm and gas-side diaphragm, exhibiting strong nonlinearity. In contrast, the thickness of the intermediate copper layer has a relatively weak influence on its stress, remaining largely stable. Considering the fatigue life and deflection performance of the diaphragm, the diaphragm thickness design should be chosen as thick as possible within the range of [0.3, 0.5 mm].

Acknowledgement: Not applicable.

Funding Statement: The work was supported by Key Science and Technology Project in Henan Province (221100240200 & 231111242200), China Postdoctoral Science Foundation (2023M733196), Youth Research Funds Plan of Zhengzhou University of Aeronautics (24ZHQN01009), Henan Provincial Department of Science and Technology Research Project (252102220065).

Author Contributions: Tao Li: established a refined numerical simulation model to analyze the mechanical properties of the diaphragm assembly under various conditions, drafted the manuscript. Wei Hu: explored how the diaphragm thickness affects stress distribution and fatigue life, drew and beautified the graphics. Haodong Luo: investigated how temperature influences the stress levels in the diaphragm. Mingxin Li: planned and coordinated the research project and its funding, summarized the current status and existing problems of diaphragm compressors. Yudong Hou: performed validation analysis and discussion of the research results. Qingchao Sun: reviewed the manuscript and completed the final draft. All authors reviewed the results and approved the final version of the manuscript.

Availability of Data and Materials: The datasets obtained during the current work are available from the corresponding authors upon request.

Ethics Approval: Not applicable.

Conflicts of Interest: The authors declare no conflicts of interest to report regarding the present study.

References

1. Wilberforce T, El-Hassan Z, Khatib F. Developments of electric cars and fuel cell hydrogen electric cars. Int J Hydrogen Energy. 2017;42(40):25695–734. doi:10.1016/j.ijhydene.2017.07.054.
2. Wang S, Wang S. Exergy analysis and optimization of methanol generating hydrogen system for PEMFC. Int J Hydrogen Energy. 2006;31(12):1747–55. doi:10.1016/j.ijhydene.2005.12.005.
3. Li Z, Pan X, Ma J. Quantitative risk assessment on 2010 Expo hydrogen station. Int J Hydrogen Energy. 2011;36(6):4079–86. doi:10.1016/j.ijhydene.2010.12.068.
4. Balat M. Potential importance of hydrogen as a future solution to environmental and transportation problems. Int J Hydrogen Energy. 2008;33(15):4013–29. doi:10.1016/j.ijhydene.2008.05.047.
5. Li T, Li M, Zhou L, Wang H, Hu W, Zhang X. Mechanical property and sealing performance analysis of the diaphragm compressor cylinder head for the hydrogen refueling station under the mutation impact load. Rev Int De Metodos Numer Para Calc Y Diseno En Ing. 2023;39(4):46. doi:10.23967/j.rimni.2023.11.002.
6. Lv R, Zhao J, Yan D, Wang J, Zhang H, Li J. Research progress on safety risk analysis and protection of core equipment in hydrogen refueling stations. Mod Chem Ind. 2025;2:16–20,26. (In Chinese).
7. Li J, Zhang J, Kang Q, Jiang C. Team of Bayesian optimization algorithms to solve task assignment problems in heterogeneous computing systems. In: 2014 IEEE International Conference on Systems, Man and Cybernetics—SMC; 2014 Oct 5–8; San Diego, CA, USA.
8. Jia X, Chen J, Wu H, Peng X. Study on the diaphragm fracture in a diaphragm compressor for a hydrogen refueling station. Int J Hydrogen Energy. 2016;41(15):6412–21. doi:10.1016/j.ijhydene.2016.02.106.
9. Jia X, Zhao Y, Chen J, Peng X. Research on the flowrate and diaphragm movement in a diaphragm compressor for a hydrogen refueling station. Int J Hydrogen Energy. 2016;41(33):14842–51. doi:10.1016/j.ijhydene.2016.05.274.
10. Lee SJ, Sohn Y, Segu DZ, Kim CL. An evaluation of the tribological characteristics of diaphragm plates for high-pressure hydrogen gas compressor applications. Lubricants. 2023;11(9):411. doi:10.3390/lubricants11090411.
11. Li F, Liu X, Liu Z, Yu Y. Study on the influence of oil-gas pressure difference on diaphragm in diaphragm compressor. J Phys Conf Ser. 2025;2963(1):012035. doi:10.1088/1742-6596/2963/1/012035.
12. Ren S, Jia X, Jiang J, Zhang S, Zhao B, Peng X. Effect of hydraulic oil compressibility on the volumetric efficiency of a diaphragm compressor for hydrogen refueling stations. Int J Hydrogen Energy. 2022;47(34):47. doi:10.1016/j.ijhydene.2022.03.033.

13. Ren S, Jia X, Li K, Chen F, Zhang S, Shi P, et al. Enhancement performance of a diaphragm compressor in hydrogen refueling stations by managing hydraulic oil temperature. Case Stud Therm Eng. 2024;53:103905. doi:10.1016/j.csite.2023.103905.
14. Li J, Liang L, Jia X, Peng X. A new generatrix of the cavity profile of a diaphragm compressor. Proc Inst Mech Eng Part C J Mech Eng Sci. 2014;228(10):1754–66. doi:10.1177/0954406213511077.
15. Hu Y, Xu X, Wang W. A new cavity profile for a diaphragm compressor used in hydrogen fueling stations. Int J Hydrogen Energy. 2017;42(38):24458–69. doi:10.1016/j.ijhydene.2017.08.058.
16. Bayrak G. Wavelet transform-based fault detection method for hydrogen energy-based distributed generators. Int J Hydrogen Energy. 2018;43(44):20293–308. doi:10.1016/j.ijhydene.2018.06.183.
17. Li X, Chen J, Wang Z, Jia X, Peng X. A non-destructive fault diagnosis method for a diaphragm compressor in the hydrogen refueling station. Int J Hydrogen Energy. 2019;44(44):24301–11. doi:10.1016/j.ijhydene.2019.07.147.
18. Ren S, Jia X, Zhang J, Li X, Zhang S, Peng X. Diagnosis method to identify diaphragm state of diaphragm compressors for hydrogen refueling stations based on dynamic oil pressure. Int J Hydrogen Energy. 2024;49:1043–55. doi:10.1016/j.ijhydene.2023.06.214.
19. Wang Y, Brubaker K. Multi-objective model auto-calibration and reduced parameterization: exploiting gradient-based optimization tool for a hydrologic model. Environ Model Softw. 2015;70(6):1–15. doi:10.1016/j.envsoft.2015.04.001.
20. Wang Y, Xue C, Jia X, Peng X. Fault diagnosis of reciprocating compressor valve with the method integrating acoustic emission signal and simulated valve motion. Mech Syst Signal Process. 2015;56(2):197–212. doi:10.1016/j.ymssp.2014.11.002.
21. Lei J, Lin Z, Zhu Q, Han G, Li P. Analysis of diaphragm compressor exhausts volume decrease. In: 2013 Fifth International Conference on Measuring Technology and Mechatronics Automation (ICMTMA); 2013 Jan 16–17; Hong Kong, China. p. 233–5.
22. Troncoso E, Lapeña-Rey N, Gonzalez M. Design tool for offgrid hydrogen refuelling systems for aerospace applications. Appl Energy. 2016;163(21):476–87. doi:10.1016/j.apenergy.2015.05.026.
23. Tahan M. Recent advances in hydrogen compressors for use in large-scale renewable energy integration. Int J Hydrogen Energy. 2022;47(83):35275–92. doi:10.1016/j.ijhydene.2022.08.128.
24. Wang T, Jia X, Li X, Ren S, Peng X. Thermal-structural coupled analysis and improvement of the diaphragm compressor cylinder head for a hydrogen refueling station. Int J Hydrogen Energy. 2020;45(1):809–21. doi:10.1016/j.ijhydene.2019.10.199.
25. Zhao M, Zhang X, Yi D, Wu D. Optimization of diaphragm compressor membrane cavity curve based on multi-objective particle swarm optimization algorithm. Compress Technol. 2024;3:1–6. (In Chinese).
26. Li J, Jia X, Wu Z, Peng X. The cavity profile of a diaphragm compressor for a hydrogen refueling station. Int J Hydrogen Energy. 2014;39(8):3926–35. doi:10.1016/j.ijhydene.2013.12.152.
27. Yang C, Huo Y, Meng K, Zhou W, Yang J, Nan Z. Fatigue failure analysis of platform screen doors under subway aerodynamic loads using finite element modeling. Eng Fail Anal. 2025;174(12):109502. doi:10.1016/j.engfailanal.2025.109502.
28. Hassan S, Stoyanov S, Rajaguru P, Bailey C. Reduced-order modelling for coupled thermal-mechanical analysis and reliability assessment of power electronic modules with nonlinear material behaviours. In: 2024 IEEE 10th Electronics System-Integration Technology Conference (ESTC); 2024 Sep 11–13; Berlin/Heidelberg, Germany. p. 1–8.
29. Li T, Wen Z, Zhao B, Sun Q. A novel collaborative optimization assembly process method for multi-performance of aeroengine rotors. Int J Adv Manuf Technol. 2023;125:1827–43. doi:10.21203/rs.3.rs-1610736/v1.
30. Dehghan S, Ismail MISB, Soury E. A thermo-mechanical finite element simulation model to analyze bushing formation and drilling tool for friction drilling of difficult-to-machine materials. J Manuf Process. 2020;57:1004–18. doi:10.1016/j.jmapro.2020.08.046.